



UNIVERSITÀ POLITECNICA DELLE MARCHE
Repository ISTITUZIONALE

Efficiency evaluation of a ductless Archimedes turbine: Laboratory experiments and numerical simulations

This is the peer reviewed version of the following article:

Original

Efficiency evaluation of a ductless Archimedes turbine: Laboratory experiments and numerical simulations / Zitti, G.; Fattore, F.; Brunori, A.; Brunori, B.; Brocchini, M.. - In: RENEWABLE ENERGY. - ISSN 0960-1481. - 146:(2020), pp. 867-879. [10.1016/j.renene.2019.06.174]

Availability:

This version is available at: 11566/273202 since: 2024-04-29T16:22:32Z

Publisher:

Published

DOI:10.1016/j.renene.2019.06.174

Terms of use:

The terms and conditions for the reuse of this version of the manuscript are specified in the publishing policy. The use of copyrighted works requires the consent of the rights' holder (author or publisher). Works made available under a Creative Commons license or a Publisher's custom-made license can be used according to the terms and conditions contained therein. See editor's website for further information and terms and conditions.

This item was downloaded from IRIS Università Politecnica delle Marche (<https://iris.univpm.it>). When citing, please refer to the published version.

(Article begins on next page)

Efficiency evaluation of a ductless Archimedes turbine: laboratory experiments and numerical simulations

Zitti Gianluca^a, Brocchini Maurizio^a, Fattore Fernando^b, Brunori
Alessandro^c, Brunori Bruno^c

^a*Dipartimento di Ingegneria Civile, Edile e di Architettura (DICEA), Università
Politecnica delle Marche, Ancona, Italy*

^b*Neferti S.r.L. Milano (Consultant for), Milano, Italy*

^c*Neferti S.r.L. Milano, Milano, Italy*

Abstract

The aim of designing a new hydrokinetic turbine simple, cheap, enviromentally friendly and suitable for remote areas is pursued by studing the efficiency of an Archimedes turbine, exploiting the kinetic energy rather than a difference in water head. First, the efficiency of a hydrokinetic Archimedes turbine is studied using laboratory experiments for low TSR regime. Subsequently, numerical simulations are run to evaluate the performance coefficient of the turbine only (without frictional losses or blockage augmentation), and to extend the TSR range. Numerical simulations lead to the determination of the efficiency curve of an hydrokinetic Archimedes turbine in aligned and inclined configuration. The obtained maximum performance coefficients are compared with the ones of other hydrokinetic turbines actually in use and exploited with parametric analysis to investigate the feasibility of the proposed turbine in real applications.

Keywords: Renewable energy, Hydrokinetic turbine, Archimedes turbine, efficiency evaluation, cheap installation

1 List of symbols

- 2 A Cross section of the rotor
- 3 b Width of the channel
- 4 C_p Performace coefficient
- 5 $C_{p,t}$ Performace coefficient of the turbine only
- 6 f Friction coefficient between teflon support device and steel joint

7	F_f	Friction force on the turbine support devices
8	F_s	Reactive force on the turbine support devices
9	g	Gravitational acceleration
10	h	Water depth
11	h_t	Height of the turbine axis from the bottom
12	i	Flume inclination
13	l	Length of the experimental flume
14	L	Length of the turbine
15	m	Mass of the counterweight system
16	M_t	Torque with respect to the turbine axis
17	p	Stride length of the turbine
18	P_{diss}	Dissipated power
19	P_f	Fluid flow power
20	P_t	Power generated by the turbine
21	Q	flow rate in the channel; the subscripts <i>rect</i> and <i>circ</i> indicate the evaluation with the rectangular and circular spillways.
22		
23	r	Pulley radius at the turbine axis
24	r_i	Radius of the i -th support devices
25	R	External radius of the turbine
26	s	Displacement of the counterweight mass
27	v	Tangential velocity of the pulley at the turbine axis, and average counterweight mass lift velocity
28		
29	v_{in}	Stream flow velocity
30	α	Inclination of the blade with respect to the turbine axis
31	Δt	Time steps for the measurement of the vertical mass displacement in experiments
32		
33	η_e	Performance coefficient of the generator or alternator
34	η_f	Performance coefficient of the transmission and support system
35	ρ	Density of the fluid
36	θ	Angle of the turbine axis with the flow
37	ω	Angular velocity of the turbine

38 1. Introduction

39 One fundamental societal challenge for the coming decades is the use of
40 renewable energy resources, towards sustainable development [1]. Hydroki-
41 netic turbines is a very promising tool towards such goal, with reference to

42 all aspects (environmental, economic and social) of sustainable development,
43 since they can produce energy through sustainable consumption of natural
44 resources. In this context, the design of new hydrokinetic energy conversion
45 system is of great interest.

46 Vermaak et al. [2] highlighted the technical, economical and environmental
47 benefits of the micro-hydrokinetic river technology, which are able to operate
48 with little or no water super-elevation. To evaluate the best option for rural
49 electricity supply, a simulation program was used in [3, 4], comparing hy-
50 drokinetic power with wind, photovoltaic and diesel generator. Hydrokinetic
51 power was found to be the best option, where water resources were available,
52 being cost effective and reducing the CO₂ input in the atmosphere. There-
53 fore, these renewable technologies provide a cost effective source of electricity
54 in rural areas, where distances are large, population are small and demand
55 for energy is low. Moreover, small hydrokinetic power systems reduce the
56 number and size of the typical required infrastructures of hydropower plants
57 (as described in [5]). The absence of these permanent infrastructures 1) re-
58 duces the impacts on the ecosystem and 2) facilitates the installation and
59 maintenance in remote areas.

60 Various reviews on hydrokinetic power systems are available. For example, [6]
61 and [7] provided an overview of vertical axis and horizontal axis hydrokinetic
62 turbines; Kumar and Sarkan [8] reviewed a wider number of hydrokinetic
63 energy conversion systems; Rostami and Fernandez proposed a vertical flat
64 plate, free to rotate about a vertical axis of symmetry, to exploit the autorota-
65 tion induced by the vortex shedding [9]; Finally, a review of vertical-axis
66 autorotation current turbines is reported in [10].

67 In this context, the Archimedes screw turbine can have an important role. It
68 has been longtime used in micro hydropower plants, with very high efficien-
69 cies (up to 85%, as reported in [11], where a traditional system is described),
70 but it was classified as a reaction turbine different from hydrokinetic tur-
71 bines in the review of Okot [12]. In fact, it exploits the potential energy
72 gradient between two reservoirs and has never been employed in free flows.
73 In view of its high performance, it was also applied in ducted systems. For
74 example, Rigling, Schleicher and co-workers evaluated numerically the effi-
75 ciency of a non-uniform Archimedean spiral rotor in [13], finding the best
76 hydraulic efficiency point equal to 72%. In both traditional and ducted con-
77 ditions, the system requires a set of structures, this constituting a significant
78 environmental impact and making the use of such technology in remote areas
79 inconvenient.

80 The aim of our contribution is to investigate the possible use of the Archimedes
81 screw turbine as an axial hydrokinetic turbine, i.e. arranging the screw in
82 the fluid flow without any supply or protection system, in order to make the
83 most of advantages of the hydrokinetic turbines described above. The use
84 and optimization of an Archimedes screw as an hydrokinetic turbine comes
85 from an idea of Soc. Neferti Srl, which designed and realized several proto-
86 types of this kind of Archimedean-Type Hydrokinetic turbines. Field tests
87 showed interesting responses and suggested a rigorous study of the turbine by
88 means of more controllable laboratory and numerical simulations. The study,
89 carried out by the Hydraulic research group of the Polytechnic University of
90 Marche, aimed to evaluate the performance of the machine and to optimize
91 the fundamental design parameters. The idea of an effective Archimedes hy-
92 drokinetic turbine aims at producing a device that: 1) is simple and cheap,
93 therefore it can be used in remote areas and developing countries; 2) mini-
94 mizes all environmental impacts; 3) does not require the construction of civil
95 infrastructures (intake and discharge reservoirs, by-pass channels, etc.); 4)
96 works also in channels and rivers with small water depths and 5) maximizes
97 the flow energy exploitation.

98 Literature on hydrokinetic Archimedes turbines is very poor. A first at-
99 tempt of using Archimedes screw as hydrokinetic turbine was proposed by
100 Stergiopoulou and co-workers [14, 15, 16], but their works did not provide an
101 accurate efficiency evaluation of the Archimedes screw hydrokinetic turbine
102 or compared it with other hydrokinetic turbines. For that reason, in this
103 paper we provide a more robust experimental and numerical study for the
104 evaluation of the performances of a ductless two strides Archimedes turbine,
105 analyzing different performance contributions and following rigorously the
106 theory of hydrokinetic turbines. In particular, we consider the geometry of a
107 classical Archimedes screw, slightly modified by inclining the blades toward
108 the incoming flow, to optimize the harnessing of the flow power. The study
109 makes use of both laboratory experiments and CFD numerical simulations,
110 the latter being used to determine carefully the torque generated by the flow
111 on an Archimedes screw turbine. Since technical requirements could involve
112 the inclination of the turbine with respect to the flow, two different configura-
113 tions (aligned with the flow and inclined with the flow) have been reproduced
114 to understand which configuration provides the greater efficiency.

115 **2. Hydrokinetic turbine efficiency**

116 The use of the Archimedes screw turbine as an axial hydrokinetic turbine
 117 totally changes its operation principles: traditional Archimedes screw tur-
 118 bine exploits the difference in potential energy between two water reservoirs,
 119 whereas hydrokinetic turbines exploit the kinetic energy of the flow.
 120 Notwithstanding the geometrical differences among the various hydrokinetic
 121 turbines, the evaluation of the efficiency of an hydrokinetic turbine is based
 on Betz' one-dimensional model [17, 18], reported in Figure 1. Betz' model

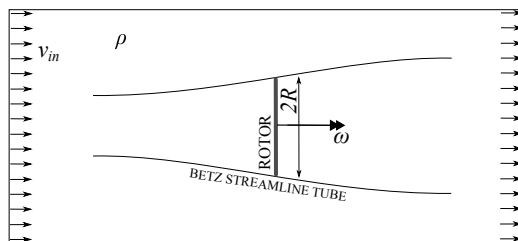


Figure 1: Sketch of Betz' model.

122 is composed by an ideal planar circular turbine with, radius R , crossed by an
 123 incompressible fluid flow with rectilinear streams of constant velocity, that
 124 leads to a rotation of the turbine with angular velocity ω . For such theory,
 125 the power available from the fluid flow P_f is:
 126

$$P_f = \frac{1}{2} \rho A v_{in}^3 \quad (1)$$

127 where ρ is the fluid density, A is the cross flow area of the turbine and v_{in}
 128 is the stream flow velocity. The performance coefficient is given by the ra-
 129 tio $C_p = P_t/P_f$, where P_t is the power generated by the screw turbine. On
 130 the basis of Betz' theory, the performance coefficient has an upper limit of
 131 0.59, but in practice several loss contributions reduces the efficiency of the
 132 turbines [19]. Betz' theory is widely used to evaluate the performance coef-
 133 ficient for wind turbines and commonly used also for more complex, three
 134 dimensional turbines. It was used in [20] to evaluate the efficiency of en-
 135 ergy conversion systems that use water currents, and in [21] as basis for a
 136 comparative evaluation of different control schemes of hydrokinetic energy
 137 conversion systems. Another interesting example is given by Schleicher et
 138 al. [22], which used both experimental and numerical simulation to design
 139 a portable micro-hydrokinetic turbine, evaluating the efficiency by means of
 140 the Betz theory.

141 In general, the performance coefficient is related to three main contribu-
 142 tions: the performace related to the turbine characteristics $C_{p,t}$, the losses
 143 related to the friction of the transmission and support system η_f , and the
 144 electrical losses in the generator or alternator η_e :

$$C_p = C_{p,t}\eta_f\eta_e \quad (2)$$

145 The performance coefficient C_p represents the dimensioness form of the tur-
 146 bine power production P_t , which depends on the turbine tip speed, i.e. on the
 147 rotation velocity and radius of the turbine. The correspondent dimensionless
 148 velocity is given by the ratio $TSR = \omega R/v_{in}$ (Tip Speed Ratio), where ω is
 149 the rotor angular velocity and R is the rotor diameter. As function of the
 150 TSR, the performance coefficients collapse onto a curve (of course, as long
 151 as the geometry and the Reynolds number range of the flow are the same).
 152 [The performance coefficient curves of some turbines as function of the Tip](#)
 153 [Speed Ratio are available in \[19\].](#)

154 Usually, the turbine performance coefficient is evaluated by measuring the
 155 power produced by the generator thus including all the three loss contribu-
 156 tions of above. Here we focus on the performance coefficient of the turbine
 157 alone, using two different approaches: laboratory experiments and numerical
 158 simulations. Experiments are designed to avoid electrical losses, but an es-
 159 timation of frictional losses is still required. Numerical simulations allow us
 160 to evaluate the power generated by the turbine alone, providing the turbine
 161 performance coefficient $C_{p,t}$.

162 In our laboratory experiments (see Figure 2 for a sketch of the experimental
 163 setup) the generated power was measured by a counterweight system, con-
 164 nected to the turbine axle, that slows down the turbine rotation. The power
 165 generated by the screw turbine P_t is obtained multiplying the counterweight
 166 force by the displacement velocity due to the turbine rotation. Then, the
 167 resultant performance coefficient obtained from the laboratory experiments
 168 is

$$C_{p,exp} = C_{p,t}\eta_f \quad (3)$$

169 where electrical losses are missing ($\eta_e = 1$), but frictional losses due to the
 170 support and counterweight systems must be evaluated to get the turbine ef-
 171 ficiency alone.

172 On the other hand, numerical simulations provided a large amount of in-
 173 formation on the flow surrounding the turbine, among which the resultant
 174 torque of the fluid pressure and the tension on the turbine surface. The

175 product of the torque by the angular velocity gave the generated power and
 176 dividing this by the available fluid power we got the performance coefficient
 177 of the turbine alone:

$$C_{p,num} = C_{p,t} \quad (4)$$

178 3. Laboratory experiments

179 The experimental apparatus (see sketch in Figure 2) was composed by an
 180 open channel with small longitudinal slope, of length $l=8$ m, width $b=0.3$ m
 181 and height of 0.3 m. The channel was made of painted steel and the sides
 182 of the flume were equipped with transparent plexiglass windows for optical
 183 measurements. The flow in the flume was generated by a pump that took
 184 water from the discharge tank and pumped it in the charge tank of the flume.
 The flume at one end is hinged to the discharge tank, while the other end is

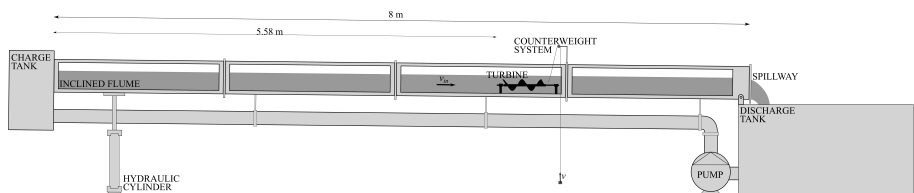


Figure 2: Sketch of the experimental setup.

185 supported by two hydraulic cylinders, that allow to vary the flume inclination
 186 between $i = 0\%$ and $i = 6.7\%$.

187 The fluid velocity v_{in} was varied by changing the flow rate in the channel
 188 and this was varied by controlling the longitudinal inclination of the flume
 189 and by using different types of spillway. The flume inclination was varied be-
 190 tween $i = 0.48\%$ and $i = 2.04\%$ when using a circular spillway and between
 191 $i = 0.48\%$ and $i = 1.6\%$ when using a rectangular spillway. The flow rates
 192 were calculated by measuring the water depth at the spillway and using the
 193 spillway theory. The rectangular spillway (0.15 m wide and 0.1 high from the
 194 flume bottom) provided a flow rate of $Q_{rect} = 8.28 \cdot 10^{-3} \text{ m}^3\text{s}^{-1}$; the circular
 195 spillway (with diameter 0.15 m and height from the flume bottom of 0.1 m)
 196 provided a flow rate of $Q_{circ} = 7.60 \cdot 10^{-3} \text{ m}^3\text{s}^{-1}$. The water depth was mea-
 197 sured for each inclination, but in the range of the used flume inclinations, the
 198

Table 1: Flume configurations with corresponding velocity and related available power P_f for the turbine in the cases aligned ($\theta = 0^\circ$) and inclined ($\theta = 10^\circ$) turbine.

ID	i [%]	Spillway	Q [m ³ s ⁻¹]	h [m]	v_{in} [ms ⁻¹]	$P_{f,\theta=0}$ [mW]	$P_{f,\theta=10}$ [mW]
F1	0.48	Circular	$7.60 \cdot 10^{-3}$	0.206	0.1239	7.4692	12.6402
F2	0.96	Circular	$7.60 \cdot 10^{-3}$	0.195	0.1309	8.8080	14.9060
F3	1.6	Circular	$7.60 \cdot 10^{-3}$	0.179	0.1426	11.3872	19.2708
F4	2.04	Circular	$7.60 \cdot 10^{-3}$	0.17	0.1502	13.3067	22.5191
F5	0.48	Rectangular	$8.28 \cdot 10^{-3}$	0.187	0.1477	12.6532	21.4132
F6	0.96	Rectangular	$8.28 \cdot 10^{-3}$	0.177	0.156	14.9085	25.2298
F7	1.6	Rectangular	$8.28 \cdot 10^{-3}$	0.162	0.1704	19.4298	32.8813

199 flow rate did not vary with the inclination. For each configuration, the water
200 depth h at several points along the water channel axis was measured and the
201 section-averaged fluid velocity was evaluated as $v_{in} = Q/bh$. The location
202 of the screw and the flume inclination have been chosen in order to have a
203 water layer over the turbine at least 20 mm thick and as far as possible from
204 the charge tank, in order to minimize its influence on the turbine. For these
205 reasons the turbine has been placed 5.58 m downstream of the charge tank.
206 The turbulence in the channel was not measured, but the Reynold number
207 was estimated as $Re \geq 25000$ for all the configurations, then the flow was
208 taken to be fully turbulent. The section-averaged flow velocities measured
209 at the turbine location ranged between $v_{in} = 0.12$ and $v_{in} = 0.17$ ms⁻¹ and
210 are reported in Table 1, together with the other experimental characteris-
211 tics. The power of the flow P_f has been evaluated with Eq. 1, where the
212 rotor area A was approximated by the projection of the turbine volume on
213 a plane perpendicular to the flow. In our case the turbine rotates inside a
214 cylindrical volume of radius R and, if the axis of the turbine is parallel to
215 the flow, the cross section area is that of a circle of radius R . If the angle
216 of the turbine axis with the flow direction is $\theta \neq 0$, the cross section area is
217 $A = R^2\pi \cos \theta + 2RL \sin \theta$, where L is the turbine length. Therefore, varying
218 the angle θ , the flow power increases because of the increase in A . Also for
219 this reason, the tests have been executed using two angles: $\theta = 0$ (aligned
220 configuration) and $\theta = 10$ (inclined configuration). Larger angles have not
221 been tested to avoid interactions of the lateral flow with the flume walls.

222 [The design of screw turbine for laboratory experiments is inspired to the](#)

223 Archimedean screw used in small hydropower plant, characterized by a scale
 224 of several meters (e.g [11]). Since the turbine object of this study is concei-
 225 ved for working without the construction of civil infrastructures, we can
 226 hypothesize that in a real application the dimension of the turbine depends
 227 on the size of the river and can range between some decimeters and several
 228 meters. Due to the geometrical geometrical of the laboratory flume, we desi-
 229 gn a turbine with radius 0.1 m and only two blade strides. The screw
 230 model (Figure 3) was made of an aluminium structural axle, to which the
 231 other parts were connected: the screw tubular axle and blades, the counter-
 weight system, and the support devices (Figure 3a). The tubular cantilever,

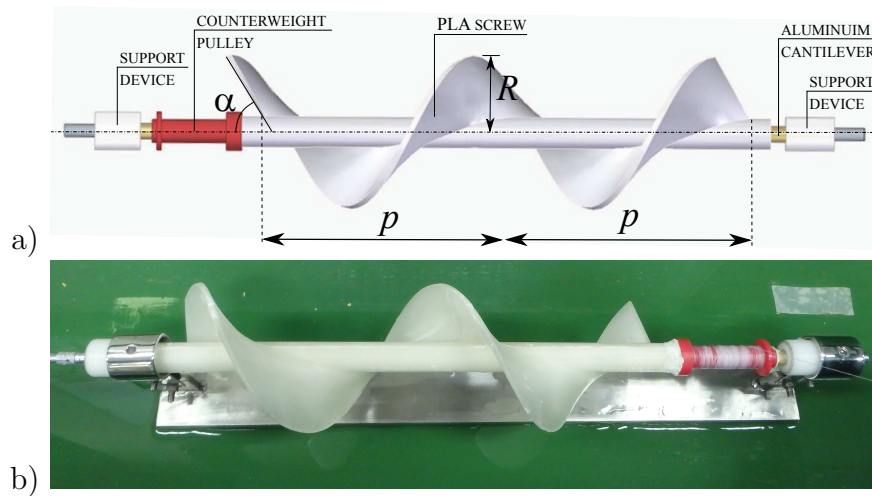


Figure 3: The screw turbine used for the experiments. a) sketch of the screw turbine model with main components; b) top view of the turbine in the support system.

232
 233 with diameter 12 mm and thickness 1 mm, provided stiffness and resistance
 234 to the screw, which was realized in polylactic acid (PLA) with a 3D printer.
 235 The screw was composed by another tubular axle and a two strides blade. It
 236 was realized in two parts, which were glued together and with the structural
 237 part using an high performance glue. The screw PLA axle had diameter of
 238 20 mm, while the blade was 5 mm thick, had external radius of $R = 50$ mm
 239 and each stride was long $p = 160$ mm. The blade was not perpendicular to
 240 the axle, but inclined of $\alpha = 70^\circ$ with respect to the turbine axis, facing
 241 the incoming flow. A summary of the main geometry parameters of the tested
 242 turbine is reported in Table 2.

243 The support devices were two teflon cylinders, with diameter 27.5 and

Table 2: Geometry parameters of the turbine.

Parameter	symbol	value
Turbine radius	R	50 mm
Axle radius	-	20 mm
Axle length	L	320 mm
Blade stride	p	160 mm
Blade inclination with respect to axle	α	70°

244 30.5 mm, connected at the extremities of the structural tube, which could be
 245 lodged in a steel support system. The support system was made of a steel
 246 plate 10 mm thick, 600 mm long and 80 mm wide, holding two spigot joints
 247 by means of small spilled plates (see Figures 3b and 4). The leeside spigot
 248 joint was equipped with an additional internal small peg, which prevented
 249 the turbine from sliding along its axis and exiting the support system during
 250 operation. The support system allowed for rotation of the support devices
 251 (and subsequently of the turbine) and located the turbine axis at $h_t=89$ mm
 252 from the bottom of the flume. The friction between the support devices and
 253 the support system was not negligible, but it was reduced as much as possible
 254 by using a teflon-steel wet interface.

255 The structural axle was equipped with a pulley for the counterweight system
 256 (Figure 4), that was made of a string with negligible stiffness, fixed at the
 257 turbine pulley and holding a mass of $m = 9$ g. The string could overpass the
 258 flume wall by means of an additional pulley fixed to the flume itself. The
 259 distance between such pulley and the ground (i.e. the maximum excursion
 260 of the counterweight system) was 1.5 m.

261 At the beginning of each test the turbine was kept still and the counterweight
 262 mass held at few centimeters above ground. When the turbine was released
 263 the video camera started recording the displacement of the conterweight mass
 264 during all its excursion with a frequency of 29.97 frs^{-1} . A dark panel and a
 265 measuring tape were put behind the mass to regard the mass itself as a target
 266 and measure the displacement s of the mass at fixed time steps of $\Delta t = 250$,
 267 in which the video was divided. Then, the lift velocity for each time step
 268 was evaluated as $v = s/\Delta t$. An example, related to test F1- $\theta 0$ is reported
 269 in Table 3. No relevant acceleration was revealed by the sensitivity of the
 270 instrument, even if in some experiments the velocity fluctuated significantly.
 271 This suggested that the rotation of the turbine is not constant, but no clear
 272 trend was inferred from the entire experimental set. Hence, the time average

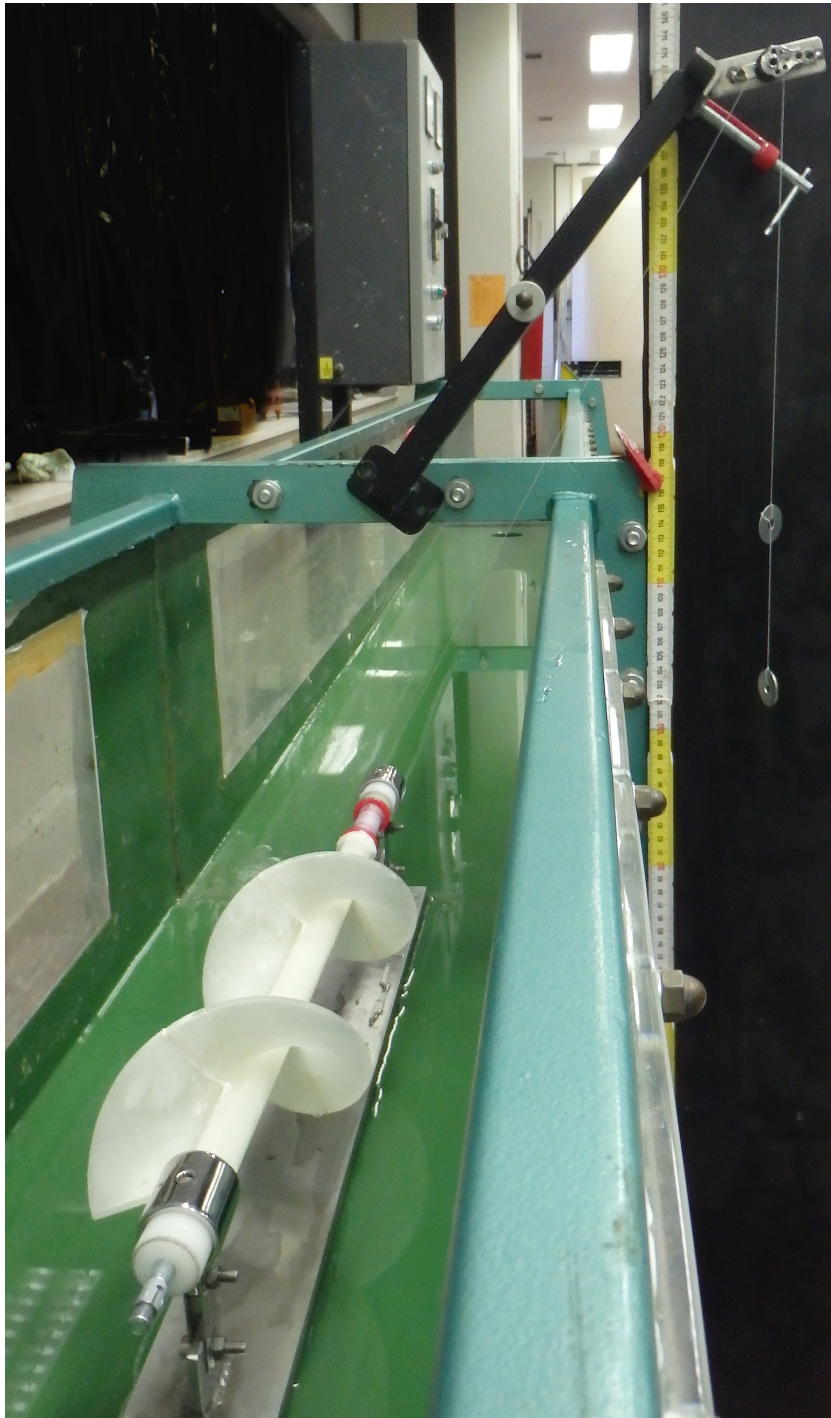


Figure 4: Perspective view of the turbine in the support system inside the flume, connected to the counterweight system (top right).

Table 3: Measured velocity for Test F1- θ

t [fr]	v [ms^{-1}]
250	$1.435 \cdot 10^{-2}$
500	$1.252 \cdot 10^{-2}$
750	$1.121 \cdot 10^{-2}$
1000	$1.235 \cdot 10^{-2}$
1250	$1.560 \cdot 10^{-2}$
1500	$1.605 \cdot 10^{-2}$
1750	$1.547 \cdot 10^{-2}$
2000	$1.260 \cdot 10^{-2}$
2250	$0.963 \cdot 10^{-2}$
2500	$1.131 \cdot 10^{-2}$
2750	$1.135 \cdot 10^{-2}$
3000	$1.083 \cdot 10^{-2}$
3250	$1.080 \cdot 10^{-2}$
3500	$1.221 \cdot 10^{-2}$
3750	$1.119 \cdot 10^{-2}$
4000	$1.329 \cdot 10^{-2}$
4250	$1.025 \cdot 10^{-2}$

Table 4: Experimental configurations and results.

ID	v_{in} [ms ⁻¹]	v [ms ⁻¹]	$\sigma(v)$ [ms ⁻¹]	ω [rads ⁻¹]	TSR [adim]	P_t [mW]	P_f [mW]	$C_{p,exp}$ [adim]	P_{diss} [mW]	$C_{p,t}$ [adim]
F1- θ	0.1239	1.249·10 ⁻²	1.02·10 ⁻³	1.67	0.1008	1.103	7.469	0.148	0.819	0.257
F2- θ	0.1309	1.510·10 ⁻²	2.18·10 ⁻³	2.01	0.1153	1.333	8.808	0.151	0.990	0.264
F3- θ	0.1426	1.636·10 ⁻²	1.34·10 ⁻³	2.18	0.1147	1.444	11.387	0.127	1.073	0.221
F4- θ	0.1502	2.052·10 ⁻²	4.12·10 ⁻³	2.74	0.1366	1.812	13.307	0.136	1.345	0.237
F5- θ	0.1477	1.333·10 ⁻²	0.81·10 ⁻³	1.78	0.0903	1.177	12.653	0.093	0.874	0.162
F6- θ	0.156	1.557·10 ⁻²	1.52·10 ⁻³	2.08	0.0998	1.375	14.908	0.092	1.021	0.161
F7- θ	0.1704	2.114·10 ⁻²	1.53·10 ⁻³	2.82	0.1241	1.867	19.430	0.096	1.386	0.167
F1- θ 10	0.1239	0.964·10 ⁻²	0.69·10 ⁻³	1.28	0.0778	0.851	12.640	0.067	0.632	0.117
F2- θ 10	0.1309	1.323·10 ⁻²	0.93·10 ⁻³	1.76	0.1011	1.168	14.906	0.078	0.867	0.137
F3- θ 10	0.1426	1.613·10 ⁻²	1.51·10 ⁻³	2.15	0.1131	1.421	19.271	0.074	1.058	0.129
F4- θ 10	0.1502	1.948·10 ⁻²	1.32·10 ⁻³	2.60	0.1297	1.720	22.519	0.076	1.277	0.133
F5- θ 10	0.1477	1.543·10 ⁻²	1.21·10 ⁻³	2.06	0.1045	1.363	21.413	0.064	1.012	0.111
F6- θ 10	0.156	1.937·10 ⁻²	1.42·10 ⁻³	2.58	0.1242	1.710	25.230	0.068	1.270	0.118
F7- θ 10	0.1704	2.271·10 ⁻²	2.58·10 ⁻³	3.03	0.1333	2.005	32.881	0.061	1.489	0.106

273 over the run duration of the measured lift velocity v was calculated. The
274 average velocity measured with this procedure corresponded to the tangential
275 velocity of the turbine pulley and was related to the turbine angular velocity
276 ω through the relation $v = \omega r$, where $r = 7.5$ mm was the radius of the
277 pulley where the string was rolled, at the turbine axis.
278 The system of above allowed one to evaluate the power generated when the
279 turbine rotated, simply multiplying the weight force of the mass by the lift
280 velocity:

$$P_t = mgv \quad (5)$$

281 where g was the gravitational acceleration.
282 Summarizing, 14 different experimental conditions were reproduced (see Ta-
283 ble 4). Each test condition was reproduced three times to check its repeata-
284 bility. The velocity averaged over such three realizations was used to evaluate
285 the power generated P_t and, subsequently, the experimental performance co-
286 efficient $C_{p,exp}$. The results are summarized in Table 4, which also gives the
287 angular velocity of the turbine ω and the TSR to be used for comparison
288 with other hydrokinetic turbines.

289 To highlight trends in the performance coefficient, the experimental results
290 have been divided into two groups, corresponding to the two different config-
291 urations (aligned and inclined), and the arithmetic means of TSR and $C_{p,exp}$
292 in each group has been calculated, providing TSR=0.1117 and $C_{p,exp} = 0.12$
293 for the aligned configuration and TSR=0.1112 and $C_{p,exp} = 0.07$ for the in-
294 clined configuration.

295 Power losses were due to the friction that developed along the contact sur-
 296 face between the moving body (teflon turbine support devices) and the fixed
 297 body (steel joints). The teflon-steel friction coefficient was taken equal to
 298 $f = 0.04$ (as reported in several engineers handbooks) and the friction force
 299 was estimated as $F_f = fF_s$, where F_s was the reaction force, equally divided
 300 between the two joints:

$$F_s = \frac{(m_t - \rho V_t)g}{2} \quad (6)$$

301 where $m_t = 0.325$ kg and $V_t = 0.239 \cdot 10^{-3}$ m³ were the turbine mass and
 302 volume respectively, while ρ was the water density. The reaction force was
 303 always the same for all experiments $F_s = 0.42$ N and produced a friction
 304 force equal to $F_f = 16.96 \cdot 10^{-3}$ N. The friction force, tangential to the joint
 305 surfaces, dissipated a power equal to

$$P_{diss} = F_f \omega (r_1 + r_2) \quad (7)$$

306 where $r_1 = 0.01375$ m and $r_2 = 0,01525$ m were the radii of the two teflon
 307 support devices. The dissipated power is reported, for each test, in the
 308 penultimate column of Table 4. The sum of the measured power $P_{t,exp}$ and
 309 dissipated power P_{diss} provided an estimate of the turbine generated power
 310 that was used to evaluate the performance coefficient of the machine alone
 311 $C_{p,t}$ (Table 4) and to extrapolate the efficiency of the support system, which
 312 is $\eta_f = 0.574$ for all the experiments. Considering both the measured and
 313 dissipated power, the set-averaged performance coefficient of the machine
 314 alone was $C_{p,t} = 0.21$ for the aligned configuration and $C_{p,t} = 0.12$ for the
 315 inclined configuration.

316 4. Numerical simulations

317 A more accurate evaluation of the performance coefficient of the machine
 318 alone $C_{p,t}$ is possible by means of dedicated numerical simulations. CFD is
 319 often used in literature to evaluate the performace coefficient of several kinds
 320 of turbines (e.g.[13, 23]). In our case, we used CFD simulations to extrapo-
 321 late the effect of the flow directly on the turbine, in terms of pressures and
 322 shear stresses and to evaluate the torque generated by the flow on the tur-
 323 bine. Numerical simulations have been performed by means of the Academic
 324 Ansys Fluent software, solving the Reynolds Averaged Navier Stokes equa-
 325 tions on a fluid domain that reproduced the geometry of the experiments

326 described in Section 3.

327 Since our goal was to evaluate the performance coefficient of the turbine
328 alone, the geometry of the laboratory turbine was reproduced in detail, the
329 support system and the countweight system were neglected and the flume
330 were substituted by a fluid domain larger than that characterizing the labo-
331 ratory experiments. This larger domain, with free slip boundary conditions,
332 aim at removing the effects of the walls, free surface and possible blockage
333 effects. In this manner, numerical simulations provided results that could
334 not be validated with experiments, but allowed us to focus on the power
335 generation of the turbine only and extend the operative condition of the tur-
336 bine to the entire possible range. In more detail, the fluid volume was a
337 parallelepiped 2 m long in the streamwise direction, 1 m wide and 0.6 m high
338 (a sketch of the horizontal plane of the domain for both configurations is
339 reported in Figure 5). The turbine was located at the center of the crossflow
340 section, at a distance of $4R$ from the inflow boundary and of $30R$ from the
341 outflow boundary, to minimize the interaction of upstream and downstream
342 hydrodynamic phenomena with the boundaries [24]. For the inclined turbine
343 the same distances were used, the center of the turbine corresponding to the
344 center of a crossflow section.

345 To generate a constant flow inside the domain the inflow-outflow boundary
346 condition were assigned at boundaries 1 (inflow) and 2 (outflow) of Figure 5.
347 To simulate a condition similar to the experiments of Section 3, the velocity
348 $v_{in} = 0.2 \text{ ms}^{-1}$ was assigned at both inflow and outflow boundaries. Free
349 slip wall boundary condition were assigned at the other four boundaries.

350 The fluid domain used in the numerical simulations was divided into two
351 parts, applying the multiple reference frame (MRF) method to include mul-
352 tiple rotating reference frames in a single domain (see Figure 5). The MFR
353 method [25] included in a single domain multiple rotating reference frames,
354 whose interface is chosen in such a way that the flow field at this location
355 is independent of the orientation of the moving parts. The calculation do-
356 main is divided into subdomains, one of which is rotating with respect to
357 the other (inertial) frame. The governing equations (mass conservation and
358 momentum conservation) in each subdomain are written with respect to that
359 subdomain's reference frame. At the boundary between two subdomains, the
360 continuity of the absolute velocity is enforced to provide the correct neighbor
361 values of velocity for the subdomain under consideration. The resulting flow
362 field was representative of a snapshot of the transient flow field in which the
363 rotating parts were moving.

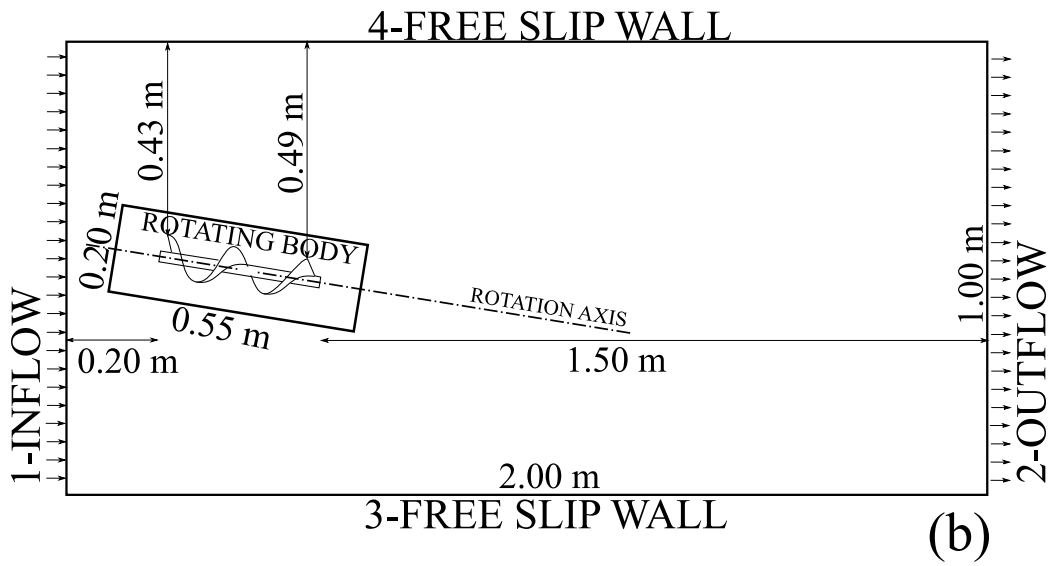
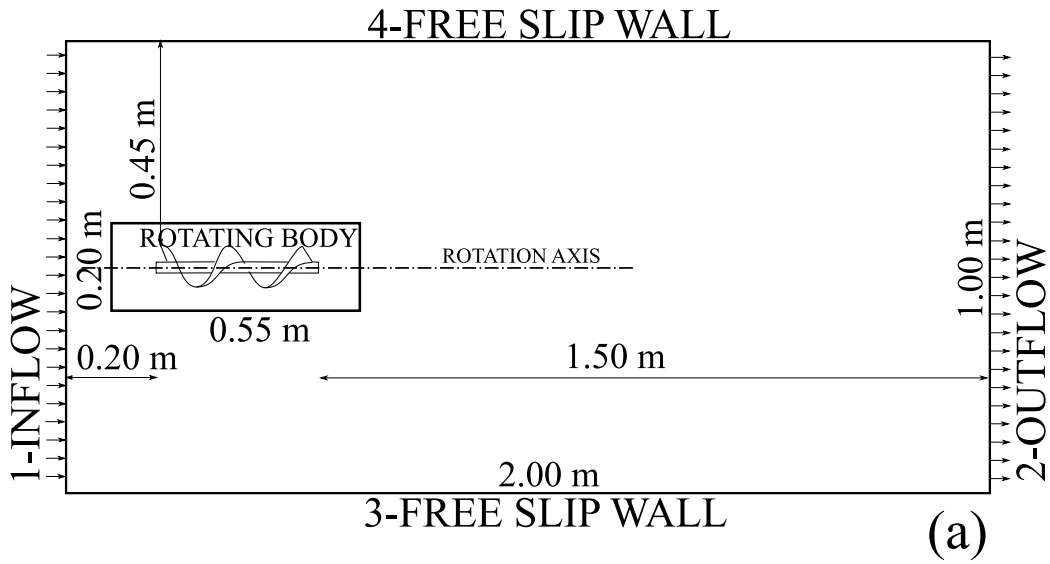


Figure 5: Sketch of the horizontal plane of the geometry of the domains used in the numerical simulations. a) aligned turbine ($\theta = 0^\circ$); b) inclined turbine ($\theta = 10^\circ$).

364 For the problem under consideration, the rotating part of the domain, here-
365 after called the rotating body, was a cylindrical volume with radius twice
366 the turbine diameter and length 0.55 m, which contained the turbine and
367 had the same axis of the turbine. The rest was the complementary to the
368 parallelepiped fluid domain. The mesh was generated separately in the two
369 parts and the rotation of the turbine was simulated moving the rotating body
370 at each time step with an assigned angular velocity ω . The solutions of the
371 two domains were calculated in the different reference frames for each part
372 and the boundary condition for the inner rotating body were evaluated by
373 interpolation on the outer body mesh.

374 The mesh, generated with Ansys Meshing Tool (ICEM CFD), was composed
375 of linear tetrahedral cells, with maximum size of $3 \cdot 10^{-2}$ m. Since the focus of
376 the simulation is the evaluation of the interaction forces on the turbine walls,
377 the mesh was refined on the surface of the screw. On the turbine surface the
378 mesh size was assigned equal to $3 \cdot 10^{-3}$ m, with an inflation perpendicular to
379 the wall that assigned a first layer thickness equal to $1 \cdot 10^{-4}$ m and increased
380 gradually the thickness for twelve layers around the turbine, with a growth
381 rate of 1.4. A representation of the refinement is given in Figure 6. The
382 above procedure led to a mesh of 157.111 nodes and 529.599 cells for the
383 flow-aligned turbine and a mesh of 141.946 nodes and 527.710 cells for the
384 10° inclined turbine. The first layer inflation at the screw wall was assigned
385 to ensure a dimensionless wall distance $y^+ < 5$, as suggested in [26] for $k - \omega$
386 Shear Stress Transport ($k - \omega$ SST) model. Because the complex geometry
387 prevented us from doing a previous estimation of the velocity gradient at the
388 wall, the value of y^+ was evaluated a posteriori for each simulation, finding a
389 y^+ smaller than 4 for all the simulations, this respecting the suggested limit
390 of $y^+ < 5$.

391 The numerical model was a pressure-based model that solved the discretized
392 form of the Reynolds Averaged Navier Stokes Equation. The turbulence
393 model used to close the equations was the Menter's $k - \omega$ Shear Stress Trans-
394 port ($k - \omega$ SST) model, which works well with adverse pressure gradients
395 and separating flow (see [27, 28, 26] for details). Some examples for the ap-
396 plication of this model, also for different condition, are given by [29, 30]

397 The two geometries of Figure 5 were used to run several simulations, differing
398 in the angular velocity of the turbine, in order to range the TSR and evaluate
399 the performance curve of the turbine for the two different configurations. For
400 each configuration, the angular velocity of the turbine was varied from 0.5 to
401 6 rads^{-1} , with steps of 0.5 rads^{-1} . Since the flow velocity is $v_{in} = 0.2 \text{ ms}^{-1}$,

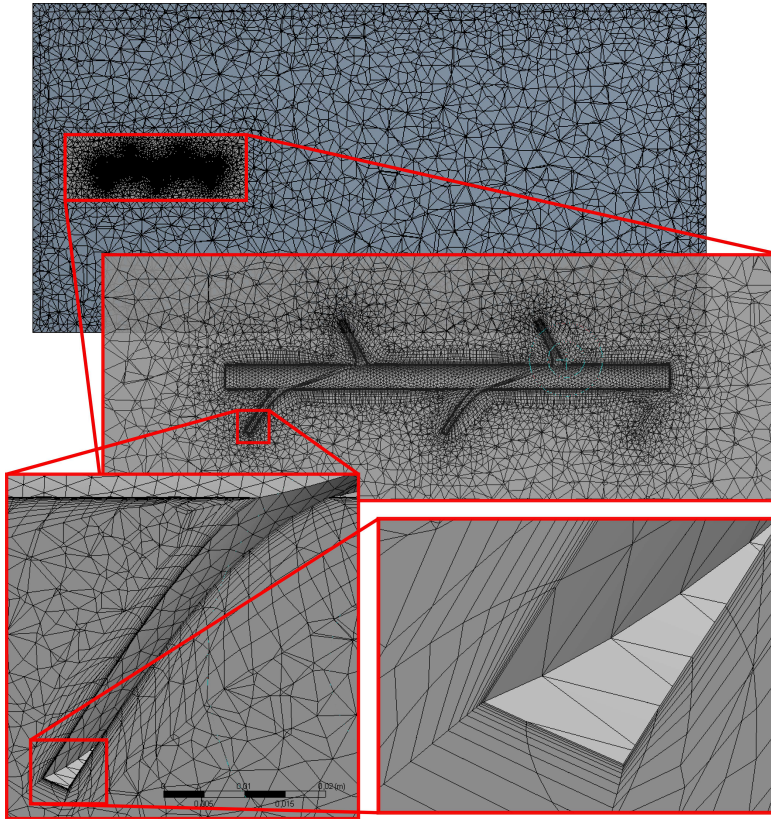


Figure 6: Zoom on the mesh refinement on the turbine surface.

402 this range of ω provides a TSR range between 0.125 and 1.5, that is suffi-
 403 cient to draw the performance curve of this kind of turbine. Each different
 404 configuration (reported in Table 6) was simulated for a total time of at least
 405 10 s, with a time step of 0.02 s. Convergence iterations at each time step
 406 were run up to a relative error of 10^{-3} for mass conservation and 10^{-4} for
 407 the velocities, with a maximum number of 50 iterations for each time step.
 408 Every ten time steps, i.e. each 0.2 s, the torque generated by the fluid on
 409 the turbine M_t was evaluated as the torque due to both pressures and shear
 410 stresses acting on the whole turbine surface with respect to the turbine axis.
 411 Figures 7a-b illustrate the torque evolution in time for all simulations. It
 412 is evident that during the initial stage a peak evolves, this caused by the
 413 transient during which the fluid-structure interaction hydrodynamics devel-
 414 ops from zero to a quasi-steady state. The time needed to achieve such

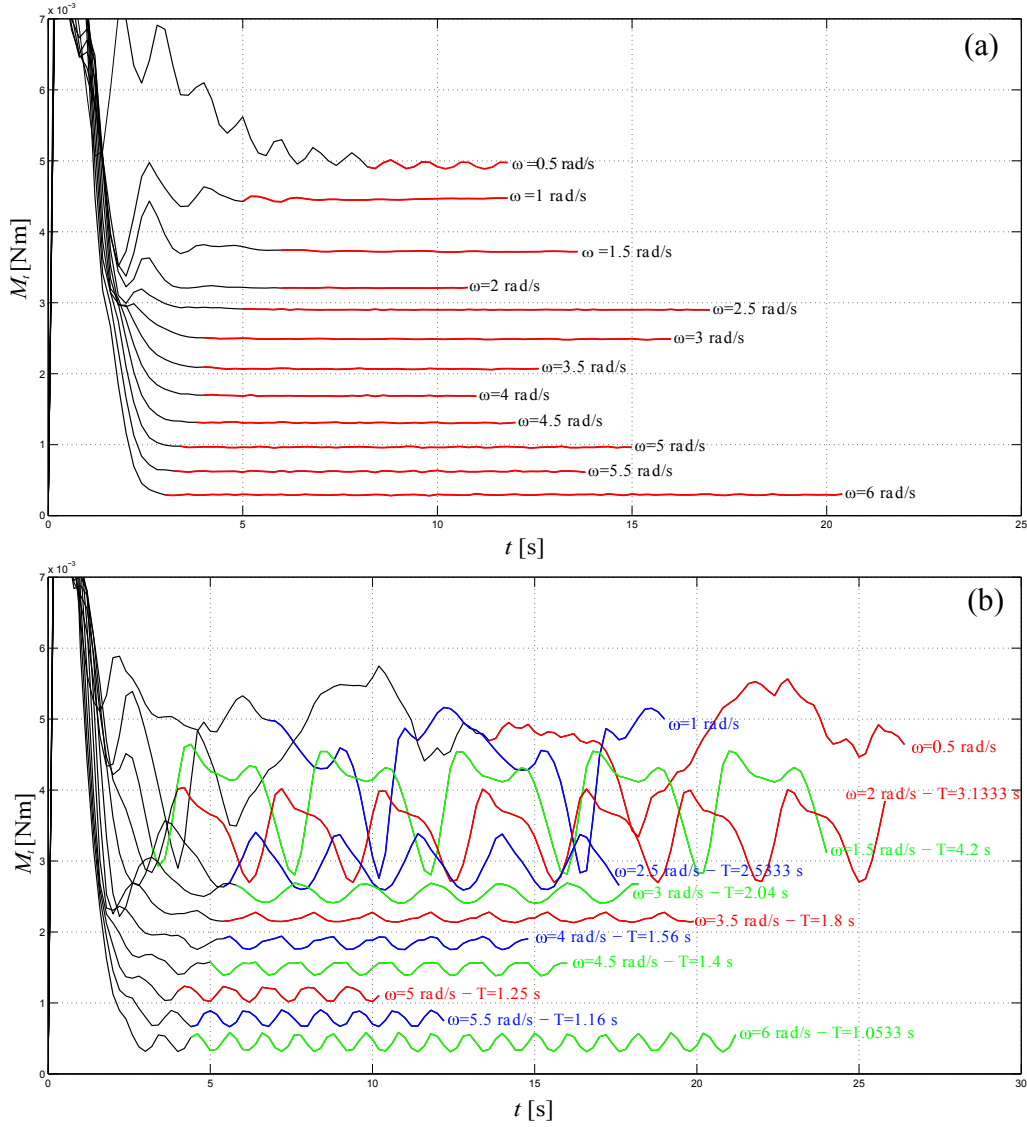


Figure 7: Evolution of the torque generated by the fluid on the turbine M_t , for each simulation, for the two configurations: a) aligned turbine ($\theta = 0^\circ$); b) inclined turbine ($\theta = 10^\circ$). At the end of each curve the angular velocity ω is reported, varied over the simulations. The coloured portions of each curve give the range used to evaluate the time-averaged torque used to calculate the performance coefficient. In panel b) the different colors are used to distinguish the curves of different simulations. For simulations with $\omega \geq 1.5$, both ω and T , evaluated over the coloured portion of the curve, are reported.

415 a quasi-steady condition (periodic oscillations in the inclined configuration)
 416 varied between 3 and 5 s. Results in this stage will be neglected in following
 417 analysis. Furthermore, for the inclined screw the torque evolution displays
 418 periodic oscillations for $\omega \geq 1.5 \text{ rads}^{-1}$ and the period of torque oscillation
 419 T was evaluated and reported in Figure 7b for each simulation. The period
 420 matches the relation $1/T = \omega/2\pi$, which is exactly the period of turbine
 421 rotation.

422 The periodic quasi-steady stage has been highlighted with colors in Figure 7
 423 and such stage has been used to evaluate a time average of the torque \bar{M}_t .
 424 The achievement of the quasi-steady state has been defined in two different
 425 ways, depending on the shape of the signal. In case of a time-invariant sig-
 426 nal, like those of Figure 7a, we required that the actual value of the variable
 427 would be within a tolerance of 10^{-4}Nm from the time-invariant value. For
 428 a periodic function, like those of Figure 7b, we implemented a Matlab rou-
 429 tine to characterize the periodicity properties (period and amplitudes) and,
 430 starting from the end of the timeseries, moved backward in time until such
 431 properties remained within a tolerance of 10^{-4}Nm .

432 To check the sensivity of the results to the mesh, we executed five tests of
 433 the same simulation, varying the characteristics of the mesh. The studied
 434 simulation was the one identified with ID 0-3 in Table 6. A summary of
 each mesh characteristics is reported in Table 5. The results of the different

Table 5: Summary of the characteristics and results of the mesh sensivity analysis. MS4 corresponds to simulation ID 0-3 in Table 6.

Simulations	MS1	MS2	MS3	MS4	MS5	MS6
Mesh type	linear	linear	quadratic	linear	linear	linear
Max. mesh size [m]	0.5	0.05	0.05	$3 \cdot 10^{-2}$	$3 \cdot 10^{-2}$	$3 \cdot 10^{-2}$
Screw surface mesh size [m]	-	-	-	$3 \cdot 10^{-3}$ m	$1.5 \cdot 10^{-3}$	10^{-3}
Inflation - 1° layer thickness [m]	-	-	-	$1 \cdot 10^{-4}$ m	$1 \cdot 10^{-5}$	$1 \cdot 10^{-6}$
Inflation - n° layers	-	-	-	12	12	12
Inflation - growth rate	-	-	-	1.4	1.4	1.4
n° nodes	15847	37688	282855	157111	542271	1215726
n° elements	84020	198767	198687	529599	1708176	3819192
\bar{M}_t [Nm]	$2.46 \cdot 10^{-3}$	$2.45 \cdot 10^{-3}$	$2.47 \cdot 10^{-3}$	$2.49 \cdot 10^{-3}$	$2.55 \cdot 10^{-3}$	$2.63 \cdot 10^{-3}$
δ	-1.2 %	-1.5%	-1%	-	+2.5 %	+5.6 %
Y_{max}^+	42	40	34	3.4	3.9	3.9

435 simulations are compared in terms of both generated torque M_t , illustrated
 436 in Figure 8 and time-averaged torque \bar{M}_t , reported in Table 5. Since the
 437 simualtion *MS4* is the reference simulation ID 0-3, the difference with the
 438

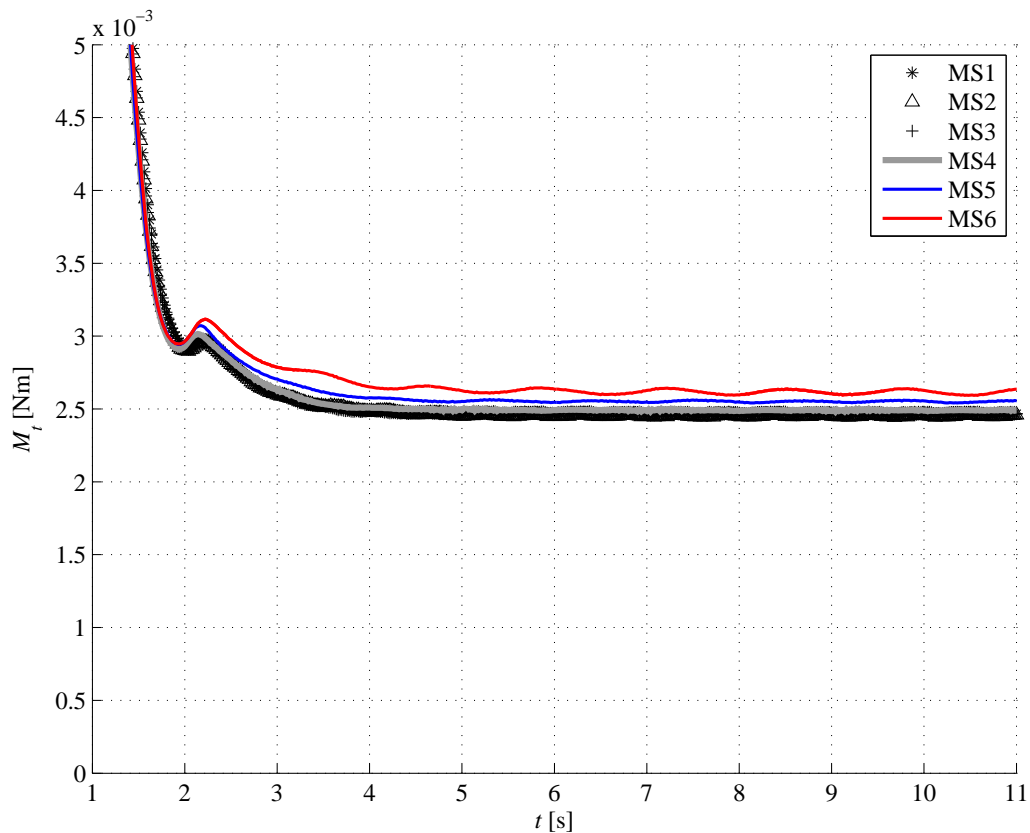


Figure 8: Results of mesh sensitivity analysis. MS4 corresponds to simulation ID 0-3 in Table 6

439 reference simulation was evaluated with

$$\delta(MSi) = \frac{\bar{M}_t(MSi) - \bar{M}_t(MS4)}{\bar{M}_t(MS4)} \quad (8)$$

440 As reported in Table 5, all the results lie in a small range around the refer-
 441 ence simulation ($\delta \in [-1.5\%, +5.6\%]$), this suggesting a small mesh sensitivity.
 442 In addition, the refined simulations provided a time-averaged torque greater
 443 than the simulation analysed in this work. Also the inclined configuration
 444 was checked: the test with $\theta = 10^\circ$ and $\omega = 2 \text{ rads}^{-1}$ was solved with a
 445 refined mesh, where the size assigned on the turbine surface was equal to
 446 $1.5 \cdot 10^{-3} \text{ m}$ and the inflation had a first layer thickness equal to $1 \cdot 10^{-5} \text{ m}$,
 447 that increased for nine layers, with a growth rate of 1.4. The refined mesh

448 had 616.415 nodes and 2.425.033. Also in this case, the simulation with the
 449 refined mesh provided a torque 5% larger than that of the simulation re-
 450 ported in this paper.

451 The influence of the time step on the simulation results was evaluated with
 452 the comparison of a reference (simulation ID 0-3 in Table 6) with two identi-
 453 cal simulations, but with different time-step size: in the first, labelled with
 454 T1 in Figure 9, the time-step size was refined with $\Delta t = 0.01$, this providing
 455 an increase in the time-averaged generated torque (evaluated with Equation
 456 8) of 1.2%; in the second, labelled with T2 in Figure 9, the time-step size was
 457 refined with $\Delta t = 0.002$ and the time-averaged generated torque increases of
 3.7%. Also in this analysis, the simulations with refined time-step size pro-

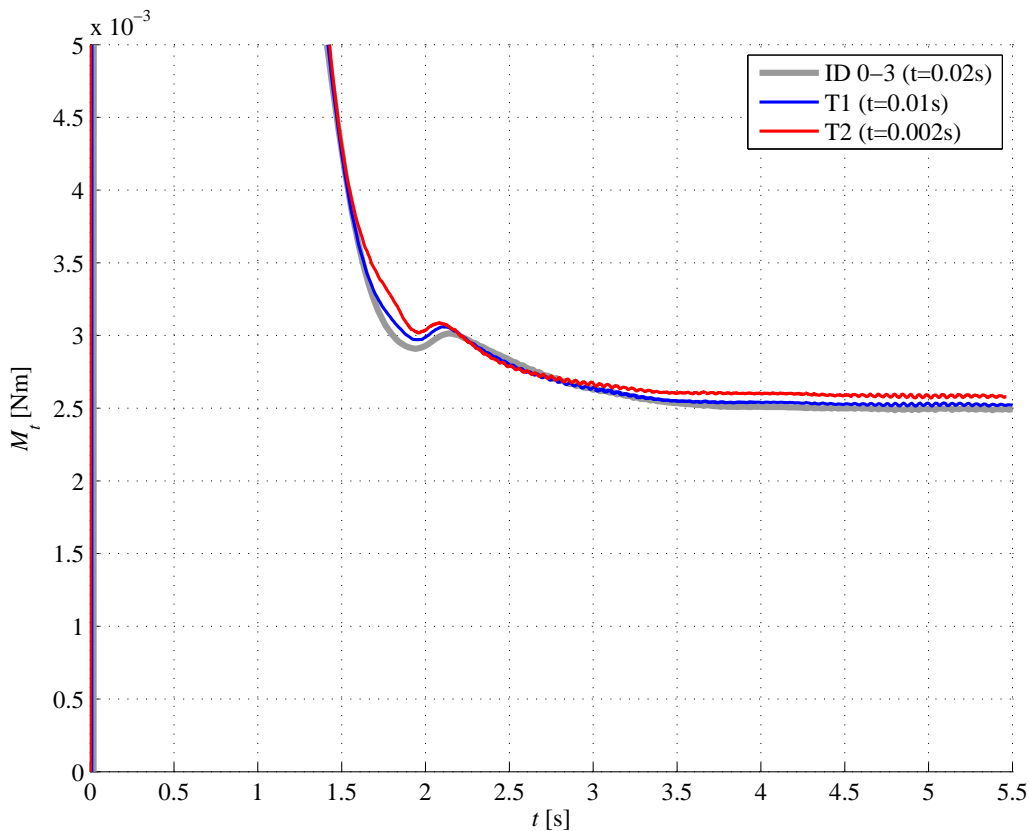


Figure 9: Results of time-step size sensitivity analysis.

458
 459 vided time-averaged torque in a small range around the reference simulation
 460 ($\delta \leq 5\%$), suggesting a small time-step size sensitivity, and greater than the

461 time-averaged torque of the reference simulation.

462 However, such more accurate results, obtained with mesh or time-step size
463 refinement, required a computational cost not acceptable for the entire nu-
464 merical campaign. Thus, the reported torque and the power and performance
465 coefficient shown below are slightly underestimated, but this does not invali-
466 date the discussion of the results.

467 The power produced by the turbine has been evaluated as

$$P_t = \bar{M}_t \omega \quad (9)$$

468 The generated powers P_t are reported in Figure 10, showing that they are
469 similar for the two configurations. Best fit of each configuration have been
470 obtained using the Nonlinear Least Squares (NLS) regression, that solves
471 nonlinear data-fitting problems in the least-squares sense with cubic func-
472 tion passing through the origin. The fit function evaluated are: $P_t = 3.22 \cdot$
473 $10^{-2} \omega^3 - \omega^2 + 5.2 \omega$ mW for the aligned configuration and $P_t = 2.66 \cdot 10^{-2} \omega^3 -$
474 $0.95 \omega^2 + 5.2 \omega$ mW for the inclined configuration, where ω is in rads^{-1} .

475 The performance coefficient has, then, been evaluated as $C_{p,num} = P_t/P_f$,
476 where the power of the flow P_f has been evaluated with equation (1) using the
477 inflow-outflow velocity of the simulation, and it was equal to $P_{f,\theta=0} = 31.42$
478 mW for the aligned configuration and to $P_{f,\theta=10} = 53.17$ mW for the inclined
479 configuration. The performance coefficients of the two configurations are
480 shown in Figure 11. Also for the performance coefficient the best fit was
481 obtained for each configuration, by using the Nonlinear Least Squares (NLS)
482 regression. The fit function evaluated are: $C_p = 0.0656\text{TSR}^3 - 0.5166\text{TSR}^2 +$
483 0.6653TSR for the aligned configuration and $C_p = 0.0321\text{TSR}^3 - 0.2881\text{TSR}^2 +$
484 0.3939TSR for the inclined configuration. For comparison, also the labora-
485 tory results are reported in Figure 11.

486 Resuming the results, the values of the time-averaged torque \bar{M}_t , the gen-
487 erated power P_t and the numerical performance coefficient $C_{p,num}$ for each
488 simulation are illustrated in Table 6.

489 5. Discussion and Conclusions

490 Results of laboratory experiments and numerical simulations showed that
491 the performance coefficients of the hydrokinetic Archimedes are in line with
492 the performances of the other hydrokinetic turbines, as reported in Table 7.
493 For this reasons the Archimedes screw turbine has such efficiency character-
494 istics that it can be assimilated to the hydrokinetic turbines actually in use

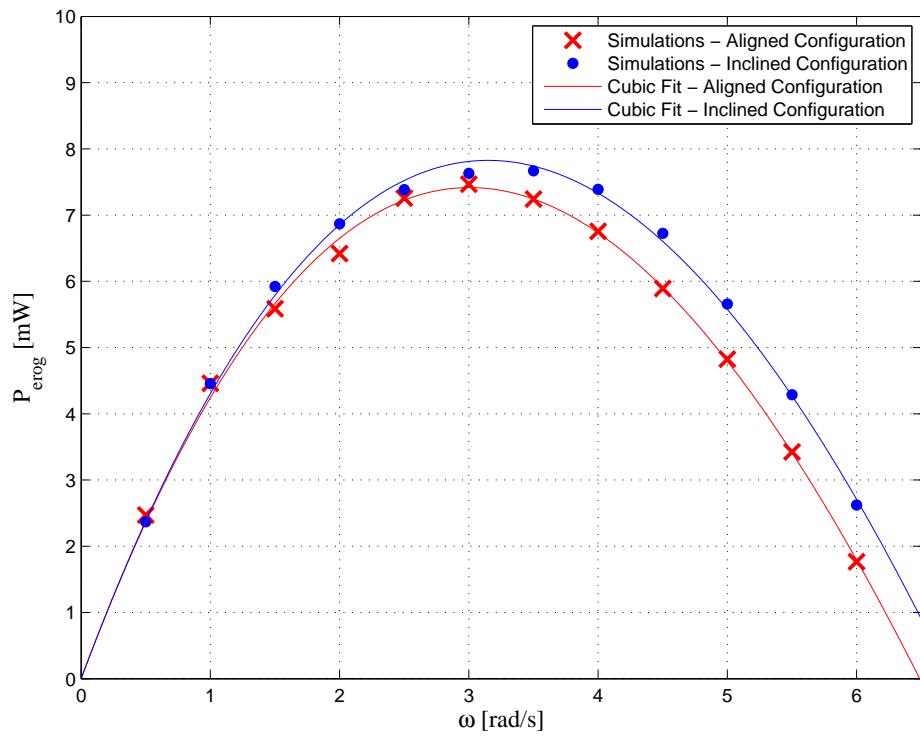


Figure 10: Generated power from numerical simulations, as function of the corresponding angular velocity ω .

Table 6: Summary of the conditions used for the numerical simulations and related results.

ID ($\theta - \omega$) grad-rads ⁻¹	TSR [adim]	\bar{M}_t [Nm]	P_t [mW]	C_p
0 - 0.5	0.125	$4.94 \cdot 10^{-3}$	2.47	0.079
0 - 1	0.25	$4.46 \cdot 10^{-3}$	4.46	0.142
0 - 1.5	0.375	$3.72 \cdot 10^{-3}$	5.59	0.178
0 - 2	0.5	$3.21 \cdot 10^{-3}$	6.42	0.204
0 - 2.5	0.625	$2.90 \cdot 10^{-3}$	7.23	0.231
0 - 3	0.75	$2.49 \cdot 10^{-3}$	7.47	0.238
0 - 3.5	0.875	$2.07 \cdot 10^{-3}$	7.24	0.231
0 - 4	1	$1.69 \cdot 10^{-3}$	6.76	0.215
0 - 4.5	1.125	$1.31 \cdot 10^{-3}$	5.89	0.188
0 - 5	1.25	$0.97 \cdot 10^{-3}$	4.83	0.154
0 - 5.5	1.375	$0.62 \cdot 10^{-3}$	3.42	0.109
0 - 6	1.5	$0.29 \cdot 10^{-3}$	1.76	0.056
10 - 0.5	0.125	$4.74 \cdot 10^{-3}$	2.37	0.045
10 - 1	0.25	$4.46 \cdot 10^{-3}$	4.46	0.084
10 - 1.5	0.375	$3.95 \cdot 10^{-3}$	5.92	0.111
10 - 2	0.5	$3.43 \cdot 10^{-3}$	6.87	0.129
10 - 2.5	0.625	$2.95 \cdot 10^{-3}$	7.38	0.139
10 - 3	0.75	$2.54 \cdot 10^{-3}$	7.63	0.144
10 - 3.5	0.875	$2.19 \cdot 10^{-3}$	7.67	0.144
10 - 4	1	$1.85 \cdot 10^{-3}$	7.39	0.139
10 - 4.5	1.125	$1.49 \cdot 10^{-3}$	6.72	0.126
10 - 5	1.25	$1.13 \cdot 10^{-3}$	5.66	0.106
10 - 5.5	1.375	$0.78 \cdot 10^{-3}$	4.29	0.081
10 - 6	1.5	$0.44 \cdot 10^{-3}$	2.62	0.049

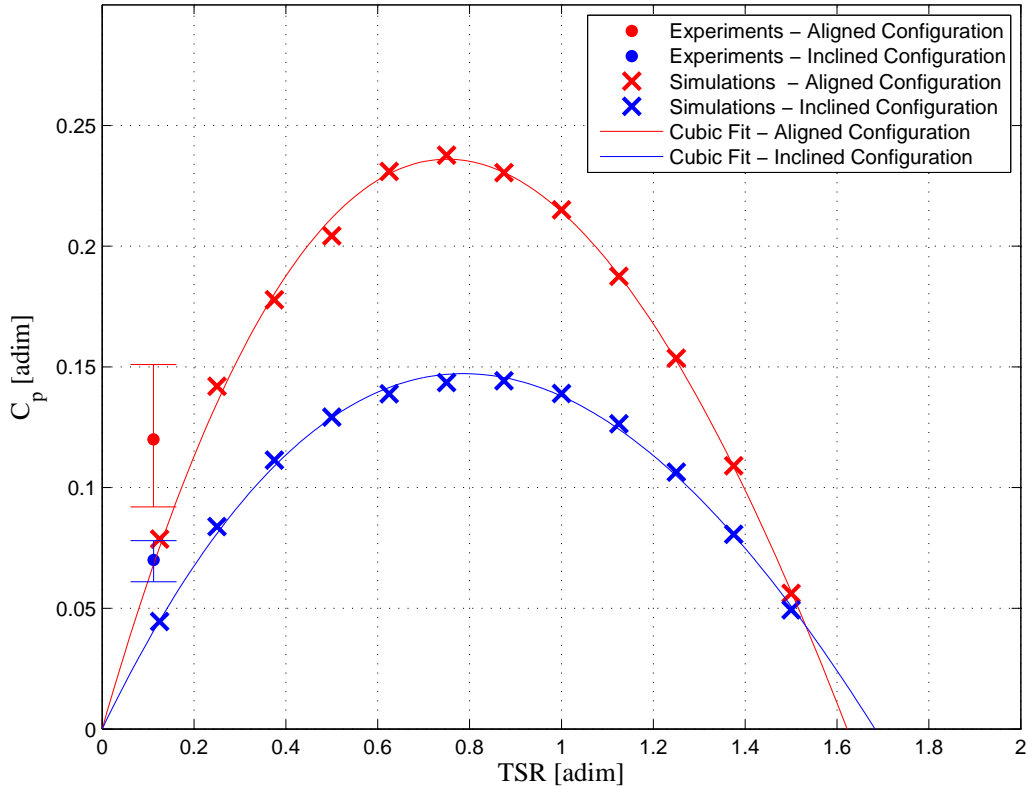


Figure 11: Power coefficient C_p as a function of the tip speed ratio for the laboratory experiments and for the numerical simulations.

495 for their ease of installation and low environmental impact.
496 Numerical and experimental results also state that the most efficient configuration is the aligned configuration. In fact, Figure 11 shows that the efficiency of the inclined configuration is smaller than that of the aligned configuration.
497
498 This is due to the fact that the flow power available for the inclined configuration is greater ($P_{f,\theta=0} = 31.42$ mW, while $P_{f,\theta=10} = 53.17$ mW), but the produced power P_t is similar. In fact, the curves of generated power in the two different configurations (see Figure 10) have not highlighted important quantitative differences for $\omega \leq 3$. For $\omega \geq 3$ the inclined configuration provides a power slightly larger than that from the aligned configuration and also the velocity range of work increases (see the cubic fit curve in Figure 10).
502
503 This is not quantitatively significant, but suggests a different interaction with the flow due to the inclination of the turbine.
504
505
506
507

Table 7: comparison of the maximum attainable performance coefficient for the Hydrokinetic Archimedes Turbine with the maximum attainable performance for some hydrokinetic turbines found in literature

Turbine type	C_p	Ref.
Axial flow turbine	0.43-0.45	[22, 24]
Rolling micro-turbines	0.55	[31]
Savonius	0.21-0.39	[32, 23]
Vertical-axis helical-bladed turbine	0.2-0.35	[33, 34]
Vertical Axis Autorotation Current Turbine	0.07	[35, 9]
Hydrokinetic Archimedes Turbine - Aligned configuration	0.238-0.264	-
Hydrokinetic Archimedes Turbine - Inclined configuration	0.144-0.167	-

508 In spite the performance coefficient obtained from the laboratory experiments
509 provides only one point for each configuration in Figure 11, the most evident
510 discrepancy is that the experimental efficiency is larger than that obtained
511 numerically for the same TSR. This can be explained in view of the possible
512 blockage, wall effects, that characterize the laboratory experiments: the flow
513 confinement could increase the drag on the turbine and, as a consequence,
514 the power generated by the turbine. However, the aim of numerical simula-
515 tions was not at reproducing the experiments, but at : 1) extending the TSR
516 range up to cover all the operative range of the Archimedes screw turbine and
517 2) removing the effects of walls (blockage), support system and counterweight
518 system (e.g. frictional losses). Extending the TSR, numerical simulations
519 provided the entire efficiency curves of the turbine in the aligned and in-
520 clined configuration (Figure 11), characterizing the turbine only.

521 Using the curves of performance coefficient of Figure 11, we can survey the
522 feasibility of the proposed turbine. In a real case, we can suppose a gen-
523 erator of 500 W rated power, typically sold on the market, and search for
524 the combination of turbine size (i.e. the radius R) and flow velocity v which
525 ensure the work of the alternator. A parametric study is carried out, varying
526 the flow velocity in the range (0, 3) m/s and considering five different radius,
527 between $R = 0.05$ m (as in the numerical simulation) and $R = 1$ m. Using
528 a Matlab code, the available power P_f is evaluated for both aligned and in-
529 clined configuration and the generated power P_t derived, considering the best
530 performance, i.e. $TSR = 0.75$, which correspond to $\eta = 0.238$ in the aligned
531 configuration and to $\eta = 0.144$ in the inclined configuration. The results of
532 the analysis is reported in Figure 12. Focusing on the aligned configuration,

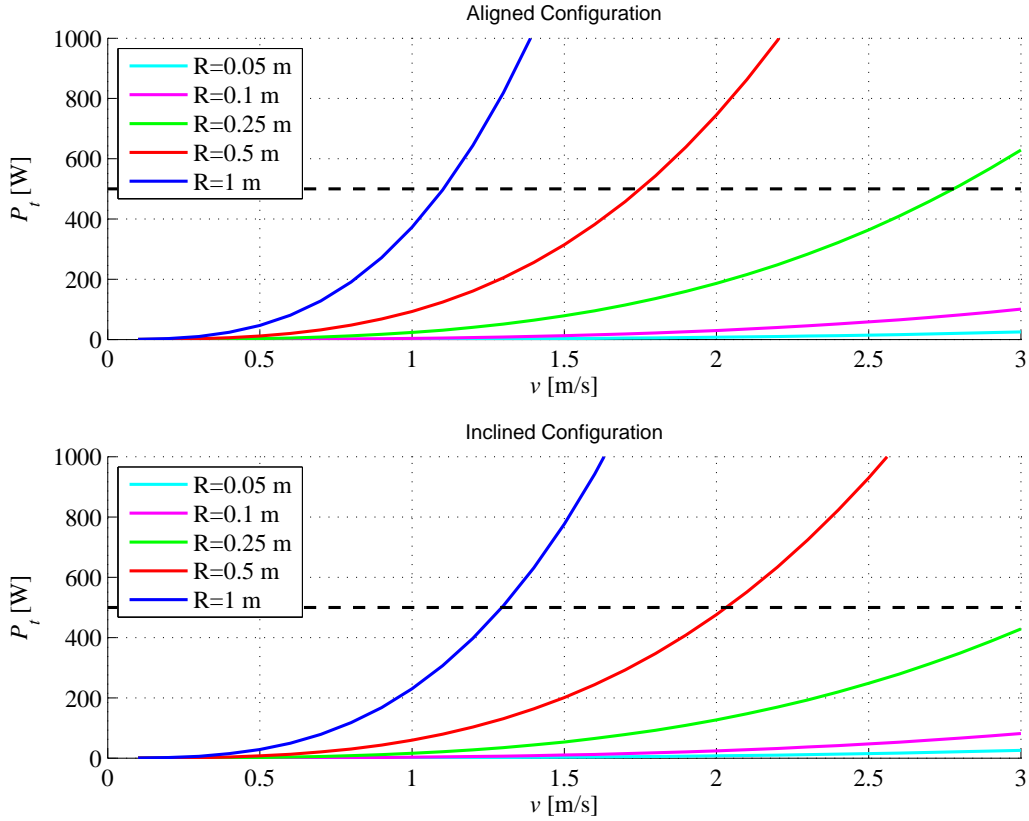


Figure 12: Power generated by Archimedean-Type Hydrokinetic turbines, with different radia R and for different water flow v .

533 it is evident that for the reference alternator functioning, a radius of at least
 534 0.25 m is necessary, and a radius of 0.5 m is required for a flow velocity lower
 535 than 2 m/s. Similar considerations can be deduced from the results of the
 536 inclined configuration, even if in this configuration faster velocities are re-
 537 quired to obtain the same P_t .

538 Efficiency curves also provide the TSR range in which the turbine is opera-
 539 tive, i.e. for $\text{TSR} \leq 1.6$, with a significant performance coefficient in the
 540 interval $0.5 \leq \text{TSR} \leq 1$. This is the same operative range of the Savonius ro-
 541 tor, showing similar efficiency (see Table 7 and [32, 23]), especially with the
 542 aligned configuration. The operative TSR range corresponds to low velocity
 543 regimes, which is an important characteristic for the compatibility with the
 544 ecosystem. In fact, if placed in river streams, low-velocity turbines induce

545 minor damages on the local fauna (i.e. fish).
546 Another interesting aspect is the periodicity of the power production, re-
547 vealed by the numerical simulations for the inclined configuration (Figure
548 7b). This periodicity is less evident for the aligned configuration. An ex-
549 planation to this aspect could related to the interaction of the turbine blades
550 with the turbulence of the generated wake. If the turbine is aligned, we can
551 suppose the generation of a wake downstream, rotating with the same axis
552 of the turbine. In this condition, the interaction between the turbine blades
553 and the wake does not vary with the rotation. Instead, if the turbine is in-
554 clined, the downstream wake would develop on a side of the rotation axis. In
555 this case the rotation of the turbine changes periodically the position of the
556 blades with respects to the wake, affecting the flow-turbine interaction and,
557 subsequently, the generated power. This is supported by the fact that the
558 generated torque period corresponds to the rotation period of the turbine T
559 , i.e. the time required to achieve the same configuration blades/wake.
560 In conclusion:

- 561 • the performance coefficient of a ductless screw turbine have been evalu-
562 ated, rigorously, for a fixed geometry and have been found comparable
563 with that of other hydrokinetic turbines characterized by the same ve-
564 locity regime;
- 565 • the inclined configuration have been found worst than the aligned con-
566 figuration, for its minor performance coefficient and for the periodicity
567 of the generated torque, still requiring a detailed analysis;
- 568 • the proposed geometry can be used in real case application with large
569 velocities or large radius.

570 For these reasons, Archimedes screw in the aligned configuration is a good
571 candidate for the development of a device simple and cheap, minimizing the
572 environmental impacts and reliable in variable water depth. Analysis is on-
573 going to further investigate the performances of this turbine in the inclined
574 configuration.

575

576 **References**

- 577 [1] U. N. G. Assembly, Resolutions and decisions adopted by the gen-
578 eral assembly during its seventieth session: Volume i 70/1 (2015).
579 doi:10.18356/25329765-en.
- 580 [2] H. J. Vermaak, K. Kusakana, S. P. Koko, Status of micro-
581 hydrokinetic river technology in rural applications: a review of
582 literature, *Renewable and Sustainable Energy Reviews* 29 (2014)
583 625–633.
- 584 [3] K. Kusakana, H. Vermaak, Feasibility study of hydrokinetic power
585 for energy access in rural south africa, in: *Proceedings of the*
586 *IASTED Asian conference, power and energy systems, 2012*, pp.
587 433–438.
- 588 [4] K. Kusakana, H. J. Vermaak, Hydrokinetic power generation for
589 rural electricity supply: Case of south africa, *Renewable energy* 55
590 (2013) 467–473.
- 591 [5] T. Price, D. Probert, Harnessing hydropower: A practical guide,
592 *Applied Energy* 57 (23) (1997) 175–251. doi:10.1016/S0306-
593 2619(97)00033-0.
- 594 [6] M. J. Khan, M. T. Iqbal, J. E. Quaicoe, River current energy
595 conversion systems: Progress, prospects and challenges, *Renew-
596 able and Sustainable Energy Reviews* 12 (8) (2008) 2177–2193.
597 doi:10.1016/j.rser.2007.04.016.
- 598 [7] M. J. Khan, G. Bhuyan, M. T. Iqbal, J. E. Quaicoe, Hydroki-
599 netic energy conversion systems and assessment of horizontal and
600 vertical axis turbines for river and tidal applications: A tech-
601 nology status review, *Applied Energy* 86 (10) (2009) 1823–1835.
602 doi:10.1016/j.apenergy.2009.02.017.
- 603 [8] D. Kumar, S. Sarkar, A review on the technology, performance,
604 design optimization, reliability, techno-economics and environ-
605 mental impacts of hydrokinetic energy conversion systems, *Re-
606 newable and Sustainable Energy Reviews* 58 (2016) 796–813.
607 doi:10.1016/j.rser.2015.12.247.

- 608 [9] A. C. Fernandes, A. B. Rostami, Hydrokinetic energy harvesting
609 by an innovative vertical axis current turbine, *Renewable Energy*
610 81 (2015) 694–706. doi:10.1016/j.renene.2015.03.084.
- 611 [10] A. B. Rostami, M. Armandei, Renewable energy harvesting by
612 vortex-induced motions: Review and benchmarking of technologies,
613 *Renewable and Sustainable Energy Reviews* 70 (2017) 193–214.
- 614 [11] Archimedean screw hydro turbine,
615 [http://www.renewablesfirst.co.uk/hydropower/hydropower-](http://www.renewablesfirst.co.uk/hydropower/hydropower-learning-centre/archimedean-screw-hydro-turbine/)
616 [learning-centre/archimedean-screw-hydro-turbine/](http://www.renewablesfirst.co.uk/hydropower/hydropower-learning-centre/archimedean-screw-hydro-turbine/) (accessed 24
617 october 2018).
- 618 [12] D. K. Okot, Review of small hydropower technology, *Renewable and Sustainable Energy Reviews* 26 (2013) 515–520.
619 doi:10.1016/j.rser.2013.05.006.
620
- 621 [13] W. Schleicher, H. Ma, J. Riglin, Z. Kraybill, W. Wei, R. Klein,
622 A. Oztekin, Characteristics of a micro-hydro turbine, *Journal of Renewable and Sustainable Energy* 6 (013119). doi:10.1063/1.4862986.
623
- 624 [14] A. Stergiopoulou, V. Stergiopoulos, E. Kalkani, Computational
625 fluid dynamics study on a 3d graphic solid model of archimedean
626 screw turbines, *Fresenius Environmental Bulletin* 23 (11) (2014)
627 2700–2706.
- 628 [15] A. Stergiopoulou, V. Stergiopoulos, E. Kalkani, Experimental
629 and theoretical research of zero head innovative horizontal axis
630 archimedean screw turbines, *International Journal of Energy and Environment* 6 (5) (2015) 471–478.
631
- 632 [16] A. Stergiopoulou, V. Stergiopoulos, E. Kalkani, Greece beyond the
633 horizon of the era of transition: Archimedean screw hydropower
634 development terra incognita, *International Journal of Energy and Environment* 6 (6) (2015) 527–536.
635
- 636 [17] A. Betz, Das maximum der theoretisch möglichen ausnützung des
637 windes durch windmotoren, *Zeitschrift für das gesamte Turbinen-*
638 *wesen* 26 (1920) 307–309.

- 639 [18] A. Betz, The maximum of the theoretically possible exploitation of
640 wind by means of a wind motor, *Wind Engineering* 37 (4) (2013)
641 441–446.
- 642 [19] M. Ragheb, A. Ragheb, Wind turbines theory the betz equation and
643 optimal rotor tip speed ratio. fundamental and advanced topics in
644 wind power, dr. rupp carriveau (ed.), intech (2011).
- 645 [20] M. S. Guney, Evaluation and measures to increase per-
646 formance coefficient of hydrokinetic turbines, *Renewable*
647 *and Sustainable Energy Reviews* 15 (8) (2011) 3669–3675.
648 doi:doi:10.1016/j.rser.2011.07.009.
- 649 [21] M. J. Khan, M. T. Iqbal, J. E. Quaicoe, Evaluation of
650 maximum power point tracking in hydrokinetic energy conver-
651 sion systems, *The Journal of Engineering* 11 (2015) 331–338.
652 doi:10.1049/joe.2015.0157.
- 653 [22] W. C. Schleicher, J. D. Riglin, A. Oztekin, Numerical character-
654 ization of a preliminary portable microhydrokinetic turbine rotor
655 design, *Renewable Energy* (76) (2015) 234–241.
- 656 [23] A. Kumar, R. P. Saini, Performance analysis of a savonius hydroki-
657 netic turbine having twisted blades, *Renewable Energy* 108 (2017)
658 502–522. doi:10.1016/j.renene.2017.03.006.
- 659 [24] L. P. Chamorro, C. Hill, S. Morton, C. Ellis, R. E. A. Arndt,
660 F. Sotiropoulos, On the interaction between a turbulent open chan-
661 nel flow and an axial-flow turbine, *Journal of Fluid Mechanics* 716
662 (2013) 658–670. doi:10.1017/jfm.2012.571.
- 663 [25] ANSYS Fluent Tutorial Guide, ANSYS, Inc. Release 18.0, (2017).
- 664 [26] B. Andersson, R. Andersson, L. Håkansson, M. Mortensen,
665 R. Sudiyo, B. Van Wachem, *Computational fluid dynamics for en-*
666 *gineers*, Cambridge University Press, (2011).
- 667 [27] F. R. Menter, Improved two-equation k-omega turbulence
668 models for aerodynamic flows, *NASA Technical Memorandum*
669 103975 (1992).

- 670 [28] F. R. Menter, Two-equation eddy-viscosity turbulence models for
671 engineering applications, *AIAA journal* 32 (8) (1994) 1598–1605.
672 doi:10.2514/3.12149.
- 673 [29] Y. Hao, L. Tan, Symmetrical and unsymmetrical tip clearances on
674 cavitation performance and radial force of a mixed flow pump as
675 turbine at pump mode, *Renewable energy* 127 (2018) 368–376.
- 676 [30] Y. Liu, L. Tan, Tip clearance on pressure fluctuation intensity and
677 vortex characteristic of a mixed flow pump as turbine at pump
678 mode, *Renewable energy* 129 (2018) 606–615.
- 679 [31] V. Beran, M. Sedlcek, F. Marsk, A new bladeless hy-
680 draulic turbine, *Applied energy* (104) (2013) 978–983.
681 doi:10.1016/j.apenergy.2012.12.016.
- 682 [32] K. Golecha, T. I. Eldho, S. V. Prabhu, Influence of
683 the deflector plate on the performance of modified savo-
684 nius water turbine, *Applied Energy* 88 (9) (2011) 3207–3217.
685 doi:10.1016/j.apenergy.2011.03.025.
- 686 [33] P. K. Talukdar, V. Kulkarni, U. K. Saha, Field-testing
687 of model helical-bladed hydrokinetic turbines for smallscale
688 power generation, *Renewable Energy* (127) (2018) 158–167.
689 doi:10.1016/j.renene.2018.04.052.
- 690 [34] A. N. Gorban, A. M. Gorlov, V. M. Silantyev, Limits of the turbine
691 efficiency for free fluid flow, *Journal of energy resources technology*
692 123 (4) (2001) 311–317.
- 693 [35] A. C. Fernandes, A. B. Rostami, L. G. Canzian, S. M. Sefat, Ver-
694 tical axis current turbine (vact) and its efficiency, in: *ASME 2013*
695 *32nd International Conference on Ocean, Offshore and Arctic En-*
696 *gineering*, American Society of Mechanical Engineers, 2013, pp.
697 V008T09A051–V008T09A051.